Role of Aortic Root Motion in Fluid-Structure Interaction Simulations of Ascending Thoracic Aortic Aneurysm

Zhu, Yu; Li, Binghuan; Armour, Chlöe; Pirola, Selene; Salmasi, Yousuf; Athanasiou, Thanos; O'Regan, Declan P.; Xu, Xiao Yun

DOI
10.1109/TBME.2025.3558436

Publication date
2025

Document Version
Final published version

Published in
IEEE Transactions on Biomedical Engineering

Citation (APA)
Zhu, Y., Li, B., Armour, C., Pirola, S., Salmasi, Y., Athanasiou, T., O'Regan, D. P., & Xu, X. Y. (2025). Role of Aortic Root Motion in Fluid-Structure Interaction Simulations of Ascending Thoracic Aortic Aneurysm. *IEEE Transactions on Biomedical Engineering*, *72*(10), 2981-2990. https://doi.org/10.1109/TBME.2025.3558436

Role of Aortic Root Motion in Fluid-Structure Interaction Simulations of Ascending Thoracic Aortic Aneurysm

Yu Zhu, Binghuan Li, Chlöe Armour, Selene Pirola, Yousuf Salmasi, Thanos Athanasiou, Declan P. O'Regan, and Xiao Yun Xu

Abstract*—*Objective: **Computational modelling of ascending thoracic aortic aneurysms (ATAA) typically assumes zero-displacement at the model's inlet. In this study we incorporated different types of aortic root motion into fluid-structure interaction (FSI) models representing an ATAA and a healthy aorta to examine their impacts on wall stress and wall shear stress (WSS) predictions.** ***Methods:*** **Five types of boundary conditions were specified at the inlet of the solid domain: (a) zero-displacement constraints, (b) longitudinal displacement, (c) in-plane displacement, (d) combined longitudinal and in-plane displacement, and (e) rotation. The aortic walls were prestressed and modelled as anisotropic hyperelastic materials. A transitional turbulence model was employed to simulate the non-Newtonian blood flow, together with patient-specific boundary conditions.** ***Results:*** **Combined longitudinal and in-plane displacement at the aortic root increased regions with elevated maximum principal stress (MPS $>$ 250 kPa) by 331% for the healthy aorta, and 57.1% for the ATAA model. Peak wall stress showed modest increases by 11.4% and 14% in the ATAA model and healthy aorta, respectively. Combined longitudinal and in-plane displacement increased the area of extremely high WSS regions ($>$20 Pa) by 20.5% in the ATAA model, primarily in the ascending aorta. For the healthy aorta, rotation had the most notable impact on WSS, reducing the area of elevated WSS regions ($>$7 Pa) by 18.8%.** ***Conclusion:*** **Our results highlight the importance of incorporating aortic root motion into FSI models for more accurate prediction of aortic wall stress and WSS. This would enhance patient-specific risk stratification for patients with ATAA.**

***Index Terms*—Aorta, ascending thoracic aortic aneurysm (ATAA), aortic root motion, fluid-structure interaction (FSI).**

I. Introduction

ATAA stands for ascending thoracic aortic aneurysm, which is a degenerative disease characterized by a permanent dilatation of a portion of the ascending aorta. As the aneurysm expands, dissection or rupture may occur, which is often lethal and has been reported as the 13th leading cause of death in Western countries [1], [2]. Surgery is typically indicated for asymptomatic ATAA patients with a maximum diameter of $\geq$ 5.5 cm [3]. However, nearly 60% of dissections occurred at diameters less than 5.5 cm [4], rendering the pressing need to identify novel predictors beyond aneurysm size for enhanced risk stratification [3].

Biomechanically, dissection or rupture can be viewed as a failure event, where wall stress exceeds the inherent strength of its tissue. Unfortunately, neither wall stress nor wall strength can be noninvasively measured *in vivo*. Image-based finite element analysis (FEA) allows personalized risk assessment through patient-specific wall stress analysis in ATAAs [5], [6], [7], [8], [9], [10]. However, these studies may have underestimated the risk of dissection or rupture due to the assumption of a fixed aortic root. Incorporating aortic root motion, particularly the axial displacement in FE models has been reported to significantly increase the longitudinal stress in the ascending aorta [11], [12], [13], [14], [15], [16], which is a known risk factor for aortic dissection. Beller et al. (2004) and Wei et al. (2019), among the others, also assessed the impact of aortic root twisting and in-plane motion on wall stress predictions. While both types of motion were found to have negligible effects on wall stress, these studies were confined to FE stress analysis of healthy aortic models [15], [16].

Patient-specific computational fluid dynamics (CFD) simulations have also been applied extensively to explore potential correlations between abnormal hemodynamic conditions within

Received 5 February 2025; revised 5 March 2025; accepted 2 April 2025. Date of publication 7 April 2025; date of current version 15 September 2025. The work of Yu Zhu was supported by British Heart Foundation under Grant FS/IPBSRF/23/27098. The work of Declan P. O'Regan was supported in part by the Medical Research Council under Grant MC_UP_1605/13 and in part by the National Institute for Health Research (NIHR) Imperial College Biomedical Research Centre and the British Heart Foundation under Grant RG/19/6/34387 and Grant RE/18/4/34215. This work was supported by Heart Research U.K. under Grant NET21-100038. *(Corresponding author: Xiao Yun Xu.)*

Yu Zhu and Chlöe Armour are with the Department of Chemical Engineering, Imperial College London, U.K, and also with the National Heart and Lung Institute, Imperial College London, U.K.

Binghuan Li is with the Department of Chemical Engineering, Imperial College London, U.K.

Selene Pirola is with the Department of Biomechanical Engineering, Delft University of Technology, The Netherlands.

Yousuf Salmasi and Thanos Athanasiou are with the Department of Surgery and Cancer, Imperial College London, U.K.

Declan P. O'Regan is with the MRC London Institute of Medical Sciences, Imperial College London, U.K.

Xiao Yun Xu is with the Department of Chemical Engineering, Imperial College London, SW7 2AZ London, U.K. (e-mail: yun.xu@imperial.ac.uk).

This article has supplementary downloadable material available at https://doi.org/10.1109/TBME.2025.3558436, provided by the authors.

Digital Object Identifier 10.1109/TBME.2025.3558436

aortic aneurysms and their progressions [17], [18], [19], [20], [21], [22], [23], [24]. High wall shear stress (WSS) has been shown to compromise the structural integrity of the aortic wall [20], [21], [22], [23], [24]. However, very few CFD studies considered the effect of aortic root motion on flow in the ascending aorta. Wendell et al. (2016) examined the impact of cardiac motion on blood flow in CFD simulations of the thoracic aorta, and by prescribing motion-compensated inflow they found that WSS was underestimated in a model without cardiac motion [25]. In another CFD study carried out by Jin et al. (2003), motion of the proximal ascending aorta was modeled by a moving wall method which incorporated radial expansion-contraction and translational movement [26]. They found that including wall motion was critical for more accurate determination of flow patterns in the ascending aorta [26]. However, longitudinal motion was not considered in this study.

The present study aimed to comprehensively examine the impacts of aortic root motion on hemodynamics and biomechanics in an ATAA model using fully coupled two-way fluid-structure interaction (FSI) simulations. Computational results, including WSS and wall mechanical stress, were compared among 5 FSI models: (1) without any root motion, (2) with longitudinal displacement only, (3) with in-plane motion only, (4) with combined longitudinal and in-plane displacement, and (5) with rotation only. These FSI simulation setups were also applied to a healthy aorta to determine whether aortic root motion has differential impacts on the parameters of interest in aneurysmal and healthy aortas.

II. Methodology

A. Data Acquisition and Geometry Reconstruction

Both computed tomography angiography (CTA) and 4D flow magnetic resonance imaging (4D-flow MRI) were performed on a patient who presented with severe aortic regurgitation and a dilated ascending aorta (maximum diameter: 5.2 cm), while only 4D-flow MRI was available for a healthy volunteer. This study received ethical approval from the Health Research Authority (HRA) in the United Kingdom (17/NI/0160).

Using Mimics 24.0 (Materialise, Leuven, Belgium), the 3D geometry of the ATAA was extracted from CTA data, while the geometry of the healthy aorta was extracted from 4D-flow images: the aorta was segmented in each three velocity phases and the magnitude phase, where different sections of the aorta could be clearly identified, before being combined into the final complete geometry. The reconstructed geometries (Fig. 1(a)) provided both the 3D fluid domain and the inner surface of the wall in the FSI model. The wall structural domain was created by uniformly offsetting the inner wall surface by 2.1 mm for the ATAA model [27] and 1.5 mm for the healthy aorta [28].

Ansys ICEM 19.2 (ANSYS, Canonsburg, PA, United States) was used to generate computational mesh for both the fluid and solid domains. For each model, the fluid domain was meshed with a tetrahedral core and 10 prismatic layers at the wall, whereas the solid domain was discretized into unstructured tetrahedral elements. The grid convergence index (GCI) was calculated to ensure the solution was mesh independent. Further details on the GCI can be found in Supplementary material S1. The final meshes comprised approximately 2.6 million elements for the fluid domain of the ATAA model and 1.2 million elements for the healthy aorta. Regarding the solid domain, the final meshes contained 1.2 and 0.8 million elements for the ATAA model and the healthy aorta, respectively.

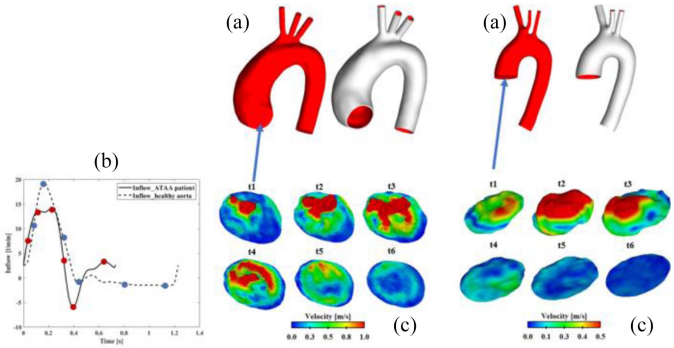

Fig. 1. (a) Reconstructed computational models for a patient with an ascending thoracic aortic aneurysm (top left) and a healthy volunteer (top right), with the fluid and solid domains shown in white and red, respectively. (b) Volumetric flow rate waveforms derived from 4D flow MRI of the ATAA patient and healthy aorta. (c) 3D inlet velocity profiles for both models at 6 time points (t1 – t6) across the cardiac cycle. Time points are indicated by red and blue circles for ATAA patient and healthy aorta, respectively, on flow rate waveforms.

B. Fluid Model

Blood flow was modelled using the Reynolds-averaged Navier-Stokes (RANS)-based shear stress transport transitional model [29], [30]. Blood was assumed to be incompressible with a constant density of 1060 kg/m^3, and its non-Newtonian behaviour was described using the empirical Carreau-Yasuda model:

$$\mu\ (\dot{\gamma}) = \mu_{\infty}\ + (\mu_0 - \ \mu_{\infty})\,(1 + (\lambda\dot{\gamma})^{a})^{\frac{n-1}{a}} \qquad (1)$$

where μ_{∞} and μ_0 are the infinite shear viscosity and the zero-shear viscosity with values being 0.0035 Pa s and 0.1600 Pa s, respectively, $\dot{\gamma}$ is the shear rate, and a, n, and λ are empirical constants with values being 0.64, 0.2128, and 8.2 s, respectively [31].

For both the ATAA and healthy aorta models, patient-specific 3D inlet velocity profiles (3D-IVPs) shown in Fig. 1(c) were applied as inlet boundary conditions. Specifically, the raw DICOM data were processed using in-house Python codes to generate complete 3D velocity fields at every time point from the 4D-flow MRI scans. The reconstructed aortic surface (Fig. 1(a)) was registered to 4D-flow MRI based on the velocity field. Using the same Python codes, the three velocity components were extracted from 4D-flow MRI at the location of the inlet and then mapped onto the meshed inlet surface. Since the MRI-derived velocity profiles correspond to an inlet plane with fixed coordinates, applying root motion at the inlet would alter its coordinates, leading to accumulated errors in the predicted inflow. To address this issue, in FSI simulations with root motion,

TABLE I
3-EWM PARAMETERS FOR MODEL OUTLETS

		R_1 [10^8 Pa s m^{-3}]	R_2 [10^8 Pa s m^{-3}]	C [10^{-9} m^3 Pa^{-1}]
ATAA patient	IA	1.29	19.79	0.91
	LCCA	1.14	17.80	1.01
	LSCA	1.01	16.10	1.12
	DA	0.11	1.39	12.82
Healthy aorta	IA	1.55	23.16	0.72
	LCCA	5.01	63.43	0.26
	LSCA	5.09	64.22	0.26
	DA	0.20	2.54	6.53

R_1 = proximal resistance, R_2 = distal resistance, C = compliance, IA = innominate artery, LCCA = left common carotid artery, LSCA = left subclavian artery, DA = descending aorta.

the coordinates defining the 3D-IVPs were manually adjusted to account for the shifted locations of the inlet planes.

The outlet boundary conditions were based on 3-element Windkessel model (3-EWM), and its parameters were tuned using patient-specific information [32]. The total blood flow through the supra-aortic branches, calculated as the difference in average flow rate, measured using 4D-flow MRI, between two planes located proximally and distally to the aortic arch, was 19% for the ATAA model and 16% for the healthy aorta. Additionally, brachial pressure measurements for the ATAA patient were recorded as 140/88 mmHg, which were then converted into central blood pressures based on the following equations [33]:

$$SBP_{central} = 0.9 * SBP_{brachial} \quad (2)$$

$$DBP_{central} = 1.01 * DBP_{brachial} \quad (3)$$

where SBP and DBP refer to systolic and diastolic blood pressure, respectively. For the healthy aorta, standard pressures of 120/80 mmHg were assumed due to the absence of pressure measurements. It should be noted that the conversion was performed by calculating the ratio of brachial to central blood pressures, based on measurements obtained and averaged over a cohort of 233 individuals [33]. However, no universally accurate method exists for converting brachial pressure to central blood pressure, as pressure amplification varies depending on factors such as age, sex, height, and individual physiology. Therefore, the exact relationship between central and brachial blood pressures varies among individuals. The calculated 3-EWM parameters for both models are reported in Table I.

C. Solid Domain

The aortic walls were described by the original Holzapfel-Gasser-Ogden (HGO) anisotropic hyperelastic material model [34]:

$$W = C_{10}(I_1 - 3) + \frac{k_1}{2k_2} \sum_{i=4,6} \left\{ \exp\left[k_2(I_i - 1)^2 - 1\right] \right\} \quad (4)$$

where W is the strain energy density, I_1 is the first deviatoric invariant, and I_4 and I_6 are the pseudo-invariants of the Green-Cauchy tensor. The material parameters, C_{10}, k_1 and k_2 were set to 109 kPa, 164.37 kPa and 4.1787 for the ATAA wall [35], and 20.9 kPa, 710 kPa and 0.4 for the healthy aortic wall [36].

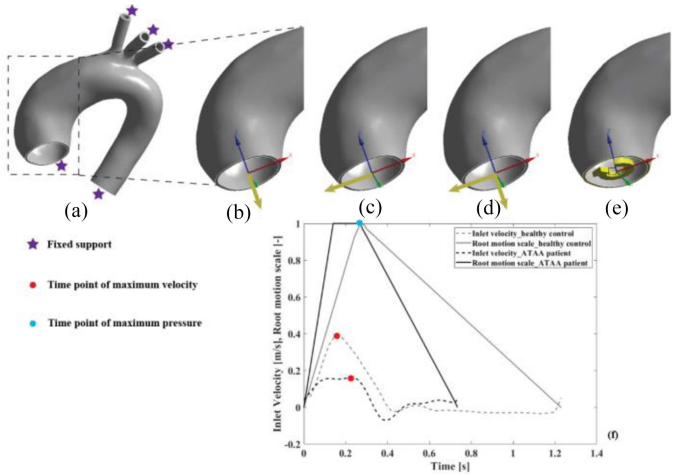

Fig. 2. Different boundary conditions applied at the inlet of the solid domain: (a) Zero-displacement, (b) Longitudinal displacement, (c) In-plane displacement, (d) Combined longitudinal and in-plane translational displacement, and (e) rotation. (f) Time-varying aortic root motion for the ATAA model (black solid line) and the healthy aorta (grey solid line) along with the corresponding inlet velocity waveforms (black and grey dashed lines). The time points corresponding to peak systole and maximum pressure are highlighted by red and blue dots, respectively.

The HGO model was implemented using Workbench APDL commands (AHYPER, EXPO). For simplicity, the two fiber families were assumed to be orthogonally aligned with the global coordinate system.

Regarding boundary conditions, zero-displacement constraints were specified at all outlets, while 5 different boundary conditions were applied at the inlet: (a) zero-displacement constraints, (b) longitudinal displacements with maximum values of 4.2 mm and 5.2 mm for the ATAA model and healthy aorta, respectively, (c) in-plane translational displacements with a peak value of 5.3 mm for the ATAA model and 5.0 mm for the healthy aorta, (d) combined longitudinal and in-plane displacements with the aforementioned peak values, and (e) clockwise rotations (viewed from proximal to distal) with a maximum value of 1.9 degrees for both models [37]. As shown in Fig. 2, a local coordinate system perpendicular to the inlet was created, and time-varying displacements and rotations were prescribed at the inlet. It should be mentioned that root motion was assumed to be linear over the cardiac cycle, with peak displacement occurring at the time point of maximum pressure. This assumption was necessary to ensure that the coordinates of 3D-IVPs can be adjusted according to the linear motion of the inlet plane. Rayleigh damping with empirical values ($\alpha = 50$, $\beta = 0.1$) was also applied to account for support provided by the surrounding tissue [38]. Prestress within the aortic walls was estimated using the procedures reported in previous studies [27], [38], [39].

D. Fluid-Structure Interaction and Numerical Details

Two-way FSI simulations, based on the arbitrary Lagrangian-Eulerian (ALE) method, were performed using ANSYS system coupling (ANSYS, Canonsburg, PA, US), which couples ANSYS Structure (solid solver) and ANSYS CFX (fluid solver) through a partitioned approach. This ensured coupling of the

fluid physics and solid physics throughout the solution process, rather than just passing data from one solver to the other at the end of the simulation. At the interface between the fluid and solid domains, the following conditions were applied: (a) displacements of the fluid and structural domain must be compatible, (b) tractions at these boundaries must be at equilibrium, and (c) the no-slip condition is still valid.

Rigid-wall CFD simulations were performed first for 7 cycles for each model to reach a periodic stable solution. The results from the last cycle were then used as the initial condition for FSI simulations, which allowed the FSI simulation to reach periodic stability within 3 cycles. A high-order advection scheme was adopted for spatial discretization of the mass and momentum conservation equations and a second-order implicit backward Euler scheme was chosen for temporal discretization, with a fixed time-step of 0.001 s. The solution convergence was controlled by setting the maximum RMS residual as 1e-5.

During the FSI simulation, the updated mesh was smoothed using the displacement diffusion method with mesh stiffness blended with distance and small volumes [40]. The motion of the inlet in the fluid model was synchronized with the structural domain. An under-relaxation factor of 0.4 was specified to dampen the pressure load transferred from the fluid solver to the solid solver during each coupling iteration, which was necessary to stabilize solutions. Within each coupled time-step (0.001 s), iterations were repeated until the maximum number of 8 iterations was reached or the data transferred between solvers converged, with the maximum RMS residual lower than 0.01. In general, the FSI simulations converged within 5 coupling time-step. Results obtained in the last cycle were used for detailed analysis. The simulation results were analyzed using CEI Ensight 10 (CEI Inc, Apex, NC, US).

III. Results

A. Comparison of FSI Results and In-Vivo Measurements

Fig. 3 presents volume-rendered instantaneous velocity fields at peak systole from both 4D-flow MRI data and FSI simulations for the ATAA model and healthy aorta. All the simulated cases (a, d, and e) showed similar flow patterns throughout the aorta for each model, indicating that the modified 3D-IVPs moved in sync with the inlet plane. The results for longitudinal and in-plane motion were not shown separately, as Case (d) captured their combined effect. Furthermore, the simulated velocities were in good overall agreement with the *in vivo* data. For the ATAA case, the high-velocity jet in the ascending aorta was well captured, although the simulated velocity magnitudes appeared lower in the descending aorta. In the healthy aorta, the high-velocity jet was accurately captured in both the ascending and descending aorta.

Fig. 4 shows detailed comparisons of velocity contours at two cross-sectional planes (CS1 and CS2) defined in the ascending aorta. Again, the results showed a good correspondence between the FSI models and 4D-flow MRI. In the ATAA model, at the plane closer to the inlet (CS1), the high-speed flow jet originated from the left side of the aorta and then impinged on the anterior wall, as shown in CS2. In the healthy aorta, the flow jet was more centered at CS1, skewing posteriorly when passing through the aortic arch.

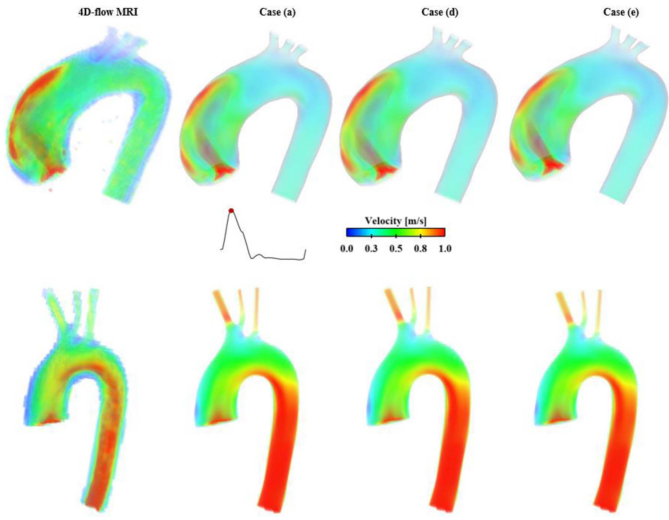

Fig. 3. Comparisons of peak systolic flow patterns across the entire fluid domain between *in vivo* 4D-flow MRI data and FSI results obtained among various simulated inlet conditions for both the ATAA model (top row) and healthy aorta (bottom row): Case (a) zero-displacement, Case (d) combined longitudinal and in-plane displacement, and Case (e) rotation.

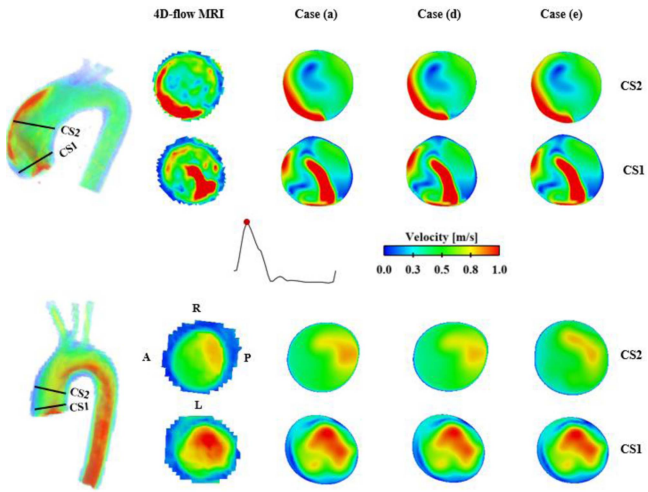

Fig. 4. Comparisons of peak systolic velocity contours at two cross-sectional planes (CS1 and CS2) between *in vivo* 4D-flow MRI data and FSI results obtained among various simulated inlet conditions for both the ATAA model (top row) and healthy aorta (bottom row): Case (a) zero-displacement, Case (d) combined longitudinal and in-plane displacement, and Case (e) rotation. A, P, R, and L represent anterior, posterior, right and left, respectively.

B. Effect of Aortic Root Motion on WSS

WSS is the frictional force induced by blood flow and healthy arterial WSS ranges between 1 and 7 Pa [41]. The spatial distributions of WSS at peak systole were comparable among the 5 simulated conditions at the aortic root, as shown in Figs. 5

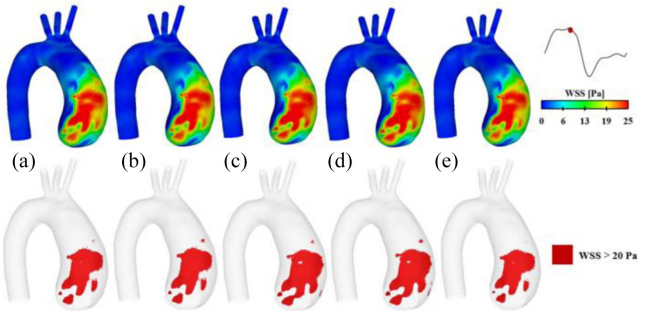

Fig. 5. Comparison of wall shear stress (WSS) distributions at peak systole were compared among 5 simulated inlet conditions for the ATAA model: (a) zero-displacement, (b) longitudinal displacement, (c) in-plane displacement, (d) combined longitudinal and in-plane displacement, and (e) rotation. The corresponding iso-surfaces were also created to show regions with elevated WSS (>20 Pa).

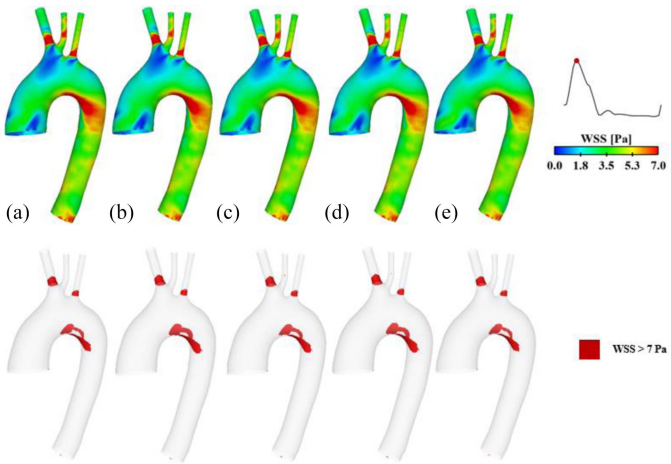

Fig. 6. Comparison of wall shear stress (WSS) distributions at peak systole were compared among 5 simulated inlet conditions for the healthy aorta: (a) zero-displacement, (b) longitudinal displacement, (c) in-plane displacement, (d) combined longitudinal and in-plane displacement, and (e) rotation. The corresponding iso-surfaces were also created to show regions with elevated WSS (>7 Pa).

and 6 for the ATAA model and the healthy aorta, respectively. For more detailed assessment of the impact of root motion on WSS, regions with elevated WSS (>20 Pa for ATAA case and >7 Pa for healthy aorta, shown in red) were illustrated by creating iso-surfaces. Again, the distributions of elevated WSS regions were similar across all the simulated models. It should be mentioned that a larger threshold of 20 Pa was used to better capture changes in extremely high WSS regions, which are more common in ATAA patients due to flow jet impingement.

Quantitative comparison of the areas of these iso-surfaces is reported in Table II, showing an opposite trend between the two cases: applying root motion increased regions with elevated WSS in the ATAA model but reduced these regions in the healthy aorta. Moreover, in contrast to the ATAA model, where an increase of elevated WSS regions occurred in the ascending aorta, the reduction in regions with elevated WSS in the healthy aorta was primarily observed along the arch. Among

TABLE II
QUANTITATIVE COMPARISON OF REGIONS WITH ELEVATED WSS

	Area (mm^2)				
	ATAA patient				
	(a)	(b)	(c)	(d)	(e)
WSS > 20 Pa	1665	1693	1997	2007	1615
	Healthy aorta				
WSS > 7 Pa	592	557	515	553	481

WSS = wall shear stress. (a) zero-displacement, (b) longitudinal displacement, (c) in-plane displacement, (d) combined longitudinal and in-plane displacement, and (e) rotation.

TABLE III
QUANTITATIVE COMPARISON OF REGIONS WITH ELEVATED WALL STRESS

	Volume (mm^3)				
	ATAA patient				
	(a)	(b)	(c)	(d)	(e)
MPS > 250 kPa	7156	8192	9062	11242	8913
	Healthy aorta				
MPS > 250 kPa	593	1402	811	2553	540

MPS = maximum principal stress. (a) zero-displacement, (b) longitudinal displacement, (c) in-plane displacement, (d) combined longitudinal and in-plane displacement, and (e) rotation.

the different types of root motion, combined longitudinal and in-plane displacement had the most significant impact on WSS, increasing the areas of regions with elevated WSS by 20.5% in the ATAA case. Conversely, in the healthy aorta, rotation resulted in the largest reduction, decreasing elevated WSS regions by 18.8%.

C. Effect of Aortic Root Motion on Wall Stress

Spatial distributions of the maximum principal stresses (MPS) are shown in Figs. 7 and 8, for the ATAA model and healthy aorta, respectively. High wall stress concentrations (indicated in red) were observed along the ascending aorta and around the arch in both models.

Iso-volumes were also created to illustrate regions with elevated MPS. In the ATAA case, all types of motion increased the areas of elevated MPS, specifically around the inner curvature of the ascending aorta. The volumes of the regions with elevated MPS were quantitatively compared across all the simulated models, with the results presented in Table III. Applying root motion increased the volumes of elevated MPS, most notably for combined longitudinal and in-plane displacement in both the ATAA model (57.1% increase) and the healthy aorta (331% increase). Interestingly, the primary contributor to elevated wall stress differed between the two models. In the ATAA model, in-plane motion alone caused a 26.6% increase in the volume of elevated MPS, compared to a 14.5% increase from longitudinal displacement. Conversely, in the healthy aorta, longitudinal motion solely led to a 136% increase in the volume of elevated MPS, while in-plane displacement resulted in a 36.8% increase. Additionally, rotation had a more pronounced impact in the ATAA model, increasing elevated MPS regions by 24.6%, while

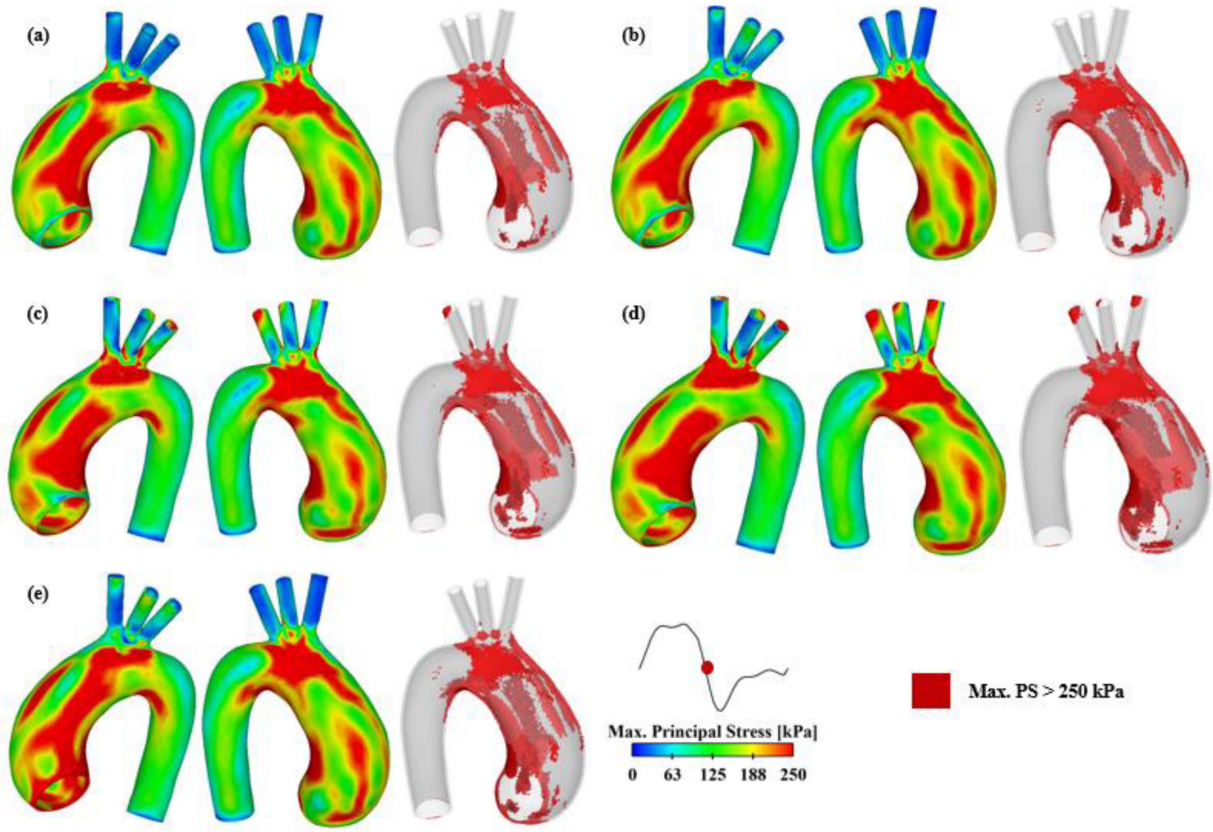

Fig. 7. Comparison of maximum principal stress (MPS) distributions at peak systole and iso-volumes of regions with MPS $>$ 250 kPa among 5 simulated inlet conditions for the ATAA model: (a) zero-displacement, (b) longitudinal displacement, (c) in-plane displacement, (d) combined longitudinal and in-plane displacement and (e) rotation.

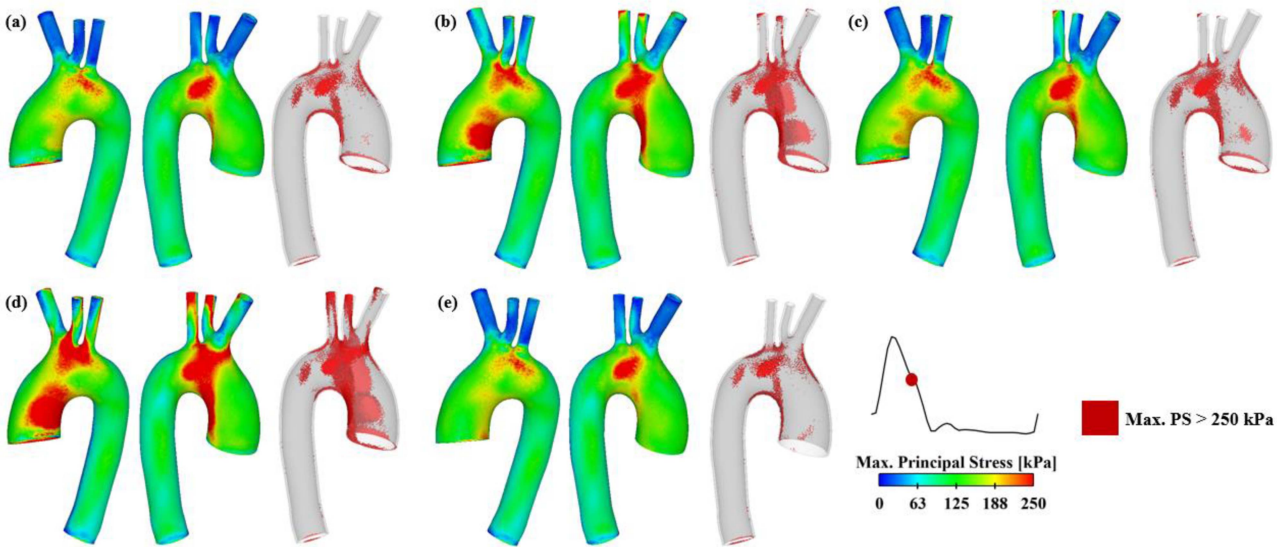

Fig. 8. Comparison of maximum principal stress (MPS) distributions at peak systole and iso-volumes of regions with MPS $>$ 250 kPa among 5 simulated inlet conditions for the healthy aorta: (a) zero-displacement, (b) longitudinal displacement, (c) in-plane displacement, (d) combined longitudinal and in-plane displacement and (e) rotation.

TABLE IV
QUANTITATIVE COMPARISON OF PEAK WALL STRESS

	ATAA patient				
	(a)	(b)	(c)	(d)	(e)
PWS (kPa)	511	518	539	569	523
	Healthy aorta				
PWS (kPa)	271	304	271	309	252

PWS = peak wall stress. (a) zero-displacement, (b) longitudinal displacement, (c) in-plane displacement, (d) combined longitudinal and in-plane displacement, and (e) rotation.

rotation in the healthy aorta caused a slight reduction (8.9%) in the volume of elevated MPS.

The peak wall stress (PWS), represented by the 99th percentile of MPS was also quantitatively compared (Table IV). Again, the most significant increase in PWS was due to combined longitudinal and in-plane displacement, resulting in an 11.4% increase in the ATAA model and a 14.0% increase in the healthy aorta.

IV. DISCUSSION

To the best of our knowledge, this is the first study to comprehensively examine the impacts of various types of aortic root motion, including longitudinal and in-plane motion, as well as rotation, on predicted WSS and wall stress simultaneously using fully coupled two-way FSI simulations. These FSI models incorporating prestress were applied to a patient with ATAA and a healthy aorta.

There has been a growing interest in quantifying the 3D-displacement and rotation of the aortic root [37], [42], which could be essential for more accurate wall stress assessments. In this study, due to the lack of patient-specific measurements, the data reported in [37] were adopted: the mean peak longitudinal displacement, in-plane displacement, and rotation angle were 4.2 mm, 5.3 mm and 1.9 degrees, respectively, for ATAA patients, and 5.2 mm, 5.0 mm, and 1.9 degrees for healthy aortas. However, inconsistencies were noted between studies [37] and [42], with study [42] reporting more significant motion, especially for rotation, with a peak angle of 11.8 degrees. Nevertheless, the data from [37] were used since they provided measurements for both healthy and aneurysmal aortas.

Recent FE studies have proposed PWS as a potential indicator for predicting the risk of rupture in patients with ATAA [5], [6], [7], [8], [9], [10]. Trabelsi et al [6], among the others, determined the rupture stress experimentally through bulge inflation tests, with values ranging from 760 kPa to 2330 kPa. However, the PWS derived from their FE analysis was much lower than the rupture stress. The underestimated wall stress could at least be partially attributed to the neglect of aortic root motion in the FE models. Introducing aortic root motion, specifically the longitudinal displacement, into the FE models has been shown to increase longitudinal stress by up to 150% in the ascending aorta [11], [12], [13], [14], [15], [16]. In the present study, applying longitudinal displacement, in-plane displacement and the combination increased PWS by 1.4%, 5.5% and 11.4%, respectively, in the ATAA model, and by 12.2%, 0.0% and 14.0% in the healthy aorta. Additionally, applying rotation increased PWS by 2.3% in the ATAA model but decreased it by 7.0% in the healthy aorta. However, simulations combining both root displacements and rotation were not performed. This decision was made not only to avoid extra model complexity and potential instability, but also to prevent nonlinear inlet motion, that could introduce errors in the 3D-IVPs.

Our results showed moderate deviations in predicted PWS with and without root motion, consistent with values (2% and 14% for two patients with aortic root dilatation) reported in [13]. However, it is evident that regions with elevated wall stress significantly increased in the models incorporating aortic root motion. [11], [12], [13], [14], [15], [16]. Therefore, we also quantitatively compared the volumes of regions with elevated wall stress, as represented by MPS. Incorporating longitudinal displacement in the ATAA model led to a 14.5% increase in the volume of regions with MPS $>$ 250 kPa. Notably, in-plane displacement had a more pronounced impact on wall stress in the ATAA model, likely due to the combined effect of the large left ventricular/aortic root angle and the highly curved ascending aorta. Consequently, applying in-plane transverse displacement also induced a substantial vertical movement of the ascending aorta, increasing the regions with elevated wall stress by 26.6%. In contrast, the healthy aorta presented with a less curved and angulated ascending aorta, showed a larger deviation (Table III) in the model with longitudinal displacement than in-plane displacement. Nevertheless, in both models, the largest deviation was observed with combined longitudinal and in-plane displacement, where the 331% increase in the healthy aorta was significantly greater than that observed in the ATAA model (57.1%), probably due to the ATAA model's stiffer wall and more curved and larger ascending aorta. Moreover, even with relatively small rotation angles (1.9 degrees) applied [37], its impact was non-trivial, particularly in the ATAA model.

WSS, acting directly on the inner surface of the blood vessels, has been reported to induce altered adaptive processes and microstructural changes in the endothelial lining of the aorta, contributing to the weakening of the aortic wall [39]. Recent studies have used 4D-flow MRI for *in vivo* estimation of WSS and identified potential associations of WSS with aortic growth and dilatation [43], [44], [45], [46]. Furthermore, a recently published work demonstrated significant correlations between time-averaged WSS (TAWSS) and circulating biomarkers of inflammation (interleukin-6) and extracellular matrix remodeling, suggesting a mechanistic link between altered hemodynamics and aortic wall degeneration [47]. Despite these findings underscore the importance of 4D flow-derived WSS in risk stratification of patients with aortic dilation, it was acknowledged that the relatively low spatial and temporal resolution of the MRI technique could affect the accuracy of WSS measurements. To overcome this limitation, patient-specific CFD analysis has been combined with 4D-flow MRI to provide high-resolution WSS estimation. Recent CFD studies on ATAAs have correlated elevated WSS with local degradation of the aortic wall's mechanical properties [20], [21], [22], [23], [24], shedding some lights on risk stratification in aneurysmal disease. However, these studies assumed a rigid aortic wall, which has been shown to influence WSS predictions [48]. By prescribing wall movement

in a patient-specific CFD model of ATAA, Perinajová et al. [49] showed that incorporating wall motion caused a mean difference of 7.47% in TAWSS, with the most significant differences observed in the ascending aorta. In the present study, TWASS was also spatially averaged over the ascending aorta and compared among FSI models with and without root motion, showing a maximum deviation of 2.4% and 3% for the ATAA model and healthy aorta, respectively.

No study in the literature has specifically assessed the sole impact of aortic root motion on predicted hemodynamics. Despite the moving wall method has been applied to incorporate the motion of both the aortic root and the aortic wall extracted from multi-phase CT/MR images [26], [49], [50], it remains unclear whether the observed differences in hemodynamics are caused by root motion or wall motion. Schussnig et al. [39] carried out a complex FSI study incorporating layer-specific anisotropic properties of the aortic wall, a non-Newtonian blood flow model, and aortic root motion (longitudinal displacement and rotation) on a patient with type B aortic dissection. However, their primary focus was on assessing the impact of wall materials on hemodynamics, and the significance of aortic root motion was not investigated.

In this study, although the spatial distributions of WSS were comparable with and without aortic root motion, quantitative comparisons revealed that incorporating root motion generally increased regions with elevated WSS in the ascending aorta of the ATAA model but reduced such regions in the aortic arch of the healthy aorta. A key flow characteristic in the ATAA model is the skewed central jet flow toward the outer curvature of the aneurysm wall. This flow impingement on the wall could cause an elevated WSS [20], [21], [22], [23], [24]. Our previous study has highlighted the importance of using 3D-IVPs to capture such characteristic in ATAA patients [51]. Therefore, we decided to simplify the root motion curves (Fig 2(c)) by assuming a linear profile, allowing the motion to be tracked and ensuring the coordinates of 3D-IVPs to be corrected accordingly. Nevertheless, since the results of interest were only compared at two specific time points rather than throughout the entire cardiac cycle, the impact of such assumption may be minimal.

Barker et al. proposed that co-localization of elevated WSS and wall stress in the dilated ascending aorta might predict catastrophic aortic events [52]. In the present study, regions of elevated WSS and MPS were both underestimated in the ATAA model without aortic root motion. In contrast to the ATAA model, the impact of root motion on WSS in the ascending aorta of the healthy aorta was negligible, likely due to the relatively uniform distribution of low and moderate WSS.

A. Limitations

First, the current study was limited by its small sample size. Our results suggested that morphological features of the ascending aorta, such as the ventricular/aortic root angle and the curvature of the ascending aorta, could influence the impact of aortic root motion on wall stress. Future studies should include a larger variety of ATAA anatomical models to better assess these effects. Second, patient-specific measurements of 3D aortic root displacements and rotations were not available and mean values for ATAA and healthy aorta along with a linear profile were adopted in our FSI simulations [37], [42], which could be integrated into our established FSI models. Previous studies have shown that aortic root motion is non-linear with a much smoother curve [53], [54]. Taking non-linear motion into consideration would necessitate auto-correction algorithms to adjust for inflow variation resulting from inlet location movements. Third, different imaging data were used to reconstruct the geometric models of the ATAA and healthy aorta due to availability. Despite the relatively low resolution of the 4D-flow MRI, it was sufficient to capture all the key features of the healthy aorta. Moreover, instead of directly comparing the simulation results between these two models, comparisons were made using the same geometric model but with varying boundary conditions. Fourth, the two fiber families in the anisotropic material model were assumed to align with the global coordinates. Aligning fibers locally would require defining local coordinate at each mesh node, leading to a significant increase in computational cost, which would not be feasible for the current study involving 10 FSI simulations. Additionally, since no specific thresholds have been reported in the literature to define 'elevated' wall stress, MPS $>$ 250 kPa was selected as wall stress in healthy aortas is typically below this value [51], [55]. Similarly, normal physiological WSS in larger arteries ranges from 1 to 7 Pa [41], hence, elevated WSS regions in the healthy aorta were defined as WSS $>$ 7 Pa. For the ATAA model, a much higher threshold of 20 Pa was selected for clearer visualization of differences across different models. We also tested various thresholds, such as 200 kPa for MPS or 7 Pa for WSS in the ATAA model and found no change in the quantitative trend. Finally, despite prestress being incorporated into our FSI simulations, the effect of longitudinal pre-stretch was neglected. which has been reported to significantly influence wall stress in young patients [56]. Its impact will be examined in our future studies.

V. Conclsuions

This study represents the first comprehensive investigation of the impacts of various types of aortic root motion, including longitudinal, in-plane displacement, and rotation, on wall stress and WSS using fully coupled two-way FSI simulations. Our FSI models, incorporating prestress, and patient-specific 3D inlet velocity profiles were applied to both an ATAA patient and a healthy aorta.

The results demonstrated that incorporating aortic root motion could strongly influence wall stress and WSS predictions. Specifically, combined longitudinal and in-plane displacement had the most pronounced effect on wall stress in both the ATAA model and the healthy aorta, leading to substantial increases in the volume of regions with elevated MPS by 57.1% and 331%, respectively. Notably, in the ATAA model, in-plane motion alone caused a 26.6% increase in the volume of elevated MPS, compared to a 14.5% increase from longitudinal displacement. Conversely, in the healthy aorta, longitudinal motion solely led to a 136% increase in the volume of elevated MPS, while in-plane displacement resulted in a 36.8% increase. The distinct

differences in biomechanical responses between the two models could be attributed to their anatomical features and different mechanical properties. Regarding WSS, applying root motion increased the area of extremely high WSS (>20 Pa) regions in the ascending aorta of the ATAA model by 20.5%, while in the healthy aorta, the area of regions with elevated WSS (>7 Pa) was reduced by 13.4%, primarily in the aortic arch.

These findings highlight the importance of incorporating aortic root motion into computational models to improve the accuracy of WSS and wall stress predictions, which are crucial for patient-specific risk stratifications of ATAA patients. Future studies will involve larger ATAA cohorts with greater anatomical variations, together with the implementation of actual root motion.

REFERENCES

[1] L. K. Bickerstaff et al., "Thoracic aortic aneurysms: A population-based study," *Surgery*, vol. 92, no. 6, pp. 1103–1108, Dec. 1982.

[2] M. A. Coady et al., "Natural history, pathogenesis, and etiology of thoracic aortic aneurysms and dissections," *Cardiol. Clin.*, vol. 17, no. 4, pp. 615–635, Nov. 1999, doi: 10.1016/S0733-8651(05)70105-3.

[3] E. M. Isselbacher et al., "2022 ACC/AHA guideline for the diagnosis and management of aortic disease: A report of the American Heart Association/American College of Cardiology Joint Committee on Clinical Practice Guidelines," *J. Amer. College Cardiol.*, vol. 80, no. 24, pp. e223–e393, Nov. 2022, doi: 10.1016/j.jacc.2022.08.004.

[4] L. A. Pape et al., "Aortic diameter≥ 5.5 cm is not a good predictor of type A aortic dissection: Observations from the International Registry of Acute Aortic Dissection (IRAD)," *Circulation*, vol. 116, no. 10, pp. 1120–1127, Aug. 2007, doi: 10.1161/CIRCULATIONAHA.107.702720.

[5] A. D. Wisneski et al., "Patient-specific finite element analysis of ascending thoracic aortic aneurysm," *J. Heart Valve Dis.*, vol. 23, no. 6, pp. 765–772, Nov. 2014.

[6] O. Trabelsi et al., "Patient specific stress and rupture analysis of ascending thoracic aneurysms," *J. Biomech.*, vol. 48, no. 10, pp. 1836–1843, Jul. 2015, doi: 10.1016/j.jbiomech.2015.04.035.

[7] Z. Wang et al., "Wall stress analyses in patients with ≥5 cm versus <5 cm ascending thoracic aortic aneurysm," *J. Thoracic Cardiovasc. Surg.*, vol. 162, no. 5, pp. 1452–1459, Nov. 2021, doi: 10.1016/j.jtcvs.2020.02.046.

[8] Y. Xuan et al., "Wall stress on ascending thoracic aortic aneurysms with bicuspid compared with tricuspid aortic valve," *J. Thoracic Cardiovasc. Surg.*, vol. 156, no. 2, pp. 492–500, Aug. 2018, doi: 10.1016/j.jtcvs.2018.03.004.

[9] A. Gomez et al., "Wall stress distribution in bicuspid aortic valve–associated ascending thoracic aortic aneurysms," *Ann. Thoracic Surg.*, vol. 110, no. 3, pp. 807–814, Sep. 2020, doi: 10.1016/j.athoracsur.2019.12.035.

[10] C. M. García–Herrera et al., "Modelling and numerical simulation of the in vivo mechanical response of the ascending aortic aneurysm in Marfan syndrome," *Med. Biol. Eng. Comput.*, vol. 55, no. 3, pp. 419–428, Mar. 2017, doi: 10.1007/s11517-016-1524-7.

[11] S. D. Singh et al., "Effects of aortic root motion on wall stress in the Marfan aorta before and after personalised aortic root support (PEARS) surgery," *J. Biomech.*, vol. 49, no. 10, pp. 2076–2084, Jul. 2016, doi: 10.1016/j.jbiomech.2016.05.011.

[12] C. J. Beller et al., "Increased aortic wall stress in aortic insufficiency: Clinical data and computer model," *Eur. J. Cardio-Thoracic Surg.*, vol. 27, no. 2, pp. 270–275, Feb. 2005, doi: 10.1016/j.ejcts.2004.11.011.

[13] D. R. Subramaniam et al., "Influence of material model and aortic root motion in finite element analysis of two exemplary cases of proximal aortic dissection," *J. Biomech. Eng.*, vol. 143, no. 1, Jan. 2021, Art. no. 014504,. doi: 10.1115/1.4048084.

[14] T. Plonek et al., "The combined impact of mechanical factors on the wall stress of the human ascending aorta–A finite elements study," *BMC Cardiovasc. Disord.*, vol. 17, pp. 1–7, Dec. 2017, doi: 10.1186/s12872-017-0733-9.

[15] W. Wei et al., "Investigating heartbeat-related in-plane motion and stress levels induced at the aortic root," *Biomed. Eng. Online*, vol. 18, pp. 1–15, Dec. 2019, doi: 10.1186/s12938-019-0632-7.

[16] C. J. Beller et al., "Role of aortic root motion in the pathogenesis of aortic dissection," *Circulation*, vol. 109, no. 6, pp. 763–769, Feb. 2004, doi: 10.1161/01.CIR.0000112569.27151.F7.

[17] U. Gülan et al., "Blood flow patterns and pressure loss in the ascending aorta: A comparative study on physiological and aneurysmal conditions," *J. Biomech.*, vol. 76, pp. 152–159, Jul. 2018, doi: 10.1016/j.jbiomech.2018.05.033.

[18] R. Jayendiran et al., "Computational prediction of hemodynamical and biomechanical alterations induced by aneurysm dilatation in patient-specific ascending thoracic aortas," *Int. J. Numer. Method Biomed. Eng.*, vol. 36, no. 6, Jun. 2020, Art. no. e3326, doi: 10.1002/cnm.3326.

[19] M. J. F. G. Ramaekers et al., "Flow patterns in ascending aortic aneurysms: Determining the role of hypertension using phase contrast magnetic resonance and computational fluid dynamics," *Comput. Biol. Med.*, vol. 172, Apr. 2024, Art. no. 108310, doi: 10.1016/j.compbiomed.2024.108310.

[20] F. Condemi et al., "Fluid-and biomechanical analysis of ascending thoracic aorta aneurysm with concomitant aortic insufficiency," *Ann. Biomed. Eng.*, vol. 45, pp. 2921–2932, Dec. 2017, doi: 10.1007/s10439-017-1913-6.

[21] F. Condemi et al., "Relationship between ascending thoracic aortic aneurysms hemodynamics and biomechanical properties," *IEEE Trans. Biomed. Eng.*, vol. 67, no. 4, pp. 949–956, Jul. 2019, doi: 10.1109/TBME.2019.2924955.

[22] D. McClarty et al., "Ascending aortic aneurysm haemodynamics are associated with aortic wall biomechanical properties," *Eur. J. Cardiothorac. Surg.*, vol. 61, no. 2, pp. 367–375, Feb. 2022, doi: 10.1093/ejcts/ezab471.

[23] S. J. Mousavi et al., "Coupling hemodynamics with mechanobiology in patient-specific computational models of ascending thoracic aortic aneurysms," *Comput. Methods Programs Biomed.*, vol. 205, Jun. 2021, Art. no. 106107, doi: 10.1016/j.cmpb.2021.106107.

[24] M. Y. Salmasi et al., "High wall shear stress can predict wall degradation in ascending aortic aneurysms: An integrated biomechanics study," *Front. Bioeng. Biotechnol.*, vol. 9, Oct. 2021, Art. no. 750656, doi: 10.3389/fbioe.2021.750656.

[25] D. C. Wendell et al., "The impact of cardiac motion on aortic valve flow used in computational simulations of the thoracic aorta," *J. Biomech. Eng.*, vol. 138, no. 9, Sep. 2016, Art. no. 091001, doi: 10.1115/1.4033964.

[26] S. Jin et al., "Effects of wall motion and compliance on flow patterns in the ascending aorta," *J. Biomech. Eng.*, vol. 125, no. 3, pp. 347–354, Jun. 2003, doi: 10.1115/1.1574332.

[27] Y. Zhu et al., "The influence of material properties and wall thickness on predicted wall stress in ascending aortic aneurysms: A finite element study," *Cardiovasc. Eng. Tech.*, vol. 16, pp. 1–14, Oct. 2024, doi: 10.1007/s13239-024-00756-9.

[28] B. Mensel et al., "MRI-based determination of reference values of thoracic aortic wall thickness in a general population," *Eur. Radiol.*, vol. 24, pp. 2038–2044, Sep. 2014, doi: 10.1007/s00330-014-3188-8.

[29] F. R. Menter et al., "A correlation-based transition model using local variables-Part i: Model formulation," *J. Turbomach.*, vol. 128, no. 3, pp. 413–422, Jul. 2006, doi: 10.1115/1.2184352.

[30] F. P. P. Tan et al., "Fluid-structure interaction analysis of wall stress and flow patterns in a thoracic aortic aneurysm," *Int. J. Appl. Mech.*, vol. 1, no. 01, pp. 179–199, Mar. 2009, doi: 10.1142/S1758825109000095.

[31] F. Abraham et al., "Shape optimization in steady blood flow: A numerical study of non-Newtonian effects," *Comput. Methods Biomech. Biomed. Eng.*, vol. 8, no. 3, pp. 127–137, Jun. 2005, doi: 10.1080/10255840500180799.

[32] S. Pirola et al., "4-D flow MRI-based computational analysis of blood flow in patient-specific aortic dissection," *IEEE Trans. Biomed. Eng.*, vol. 66, no. 12, pp. 3411–3419, Mar. 2019, doi: 10.1109/TBME.2019.2904885.

[33] J. L. Izzo Jr, "Brachial vs. central systolic pressure and pulse wave transmission indicators: A critical analysis," *Am. J. Hypertens.*, vol. 27, no. 12, pp. 1433–1442, Dec. 2014, doi: 10.1093/ajh/hpu135.

[34] G.A. Holzapfel et al., "A new constitutive framework for arterial wall mechanics and a comparative study of material models," *J. Elasticity*, vol. 61, pp. 1–48, Jul. 2000, doi: 10.1023/A:1010835316564.

[35] M.L.F. da Silva et al., "Structural numerical analysis of a branched modular stent-graft for aneurysms encompassing all zones of the aortic arch," *J. Mech. Behav. Biomed. Mater.*, vol. 147, Nov. 2023, Art. no. 106135, doi: 10.1016/j.jmbbm.2023.106135.

[36] D. Haskett et al., "Microstructural and biomechanical alterations of the human aorta as a function of age and location," *Biomech. Model. Mechanobiol.*, vol. 9, pp. 725–736, Dec. 2010, doi: 10.1007/s10237-010-0209-7.

[37] T. Kim et al., "Three-dimensional characterization of aortic root motion by vascular deformation mapping," *J. Clin. Med.*, vol. 12, no. 13, Jul. 2023, Art. no. 4471, doi: 10.3390/jcm12134471.

[38] Y. Zhu et al., "Fluid-structure interaction simulations of repaired type A aortic dissection: A comprehensive comparison with rigid wall models," *Front. Physiol.*, vol. 13, Jun. 2022, Art. no. 913457, doi: 10.3389/fphys.2022.913457.

[39] R. Schussnig et al., "On the role of tissue mechanics in fluid–structure interaction simulations of patient-specific aortic dissection," *Int. J. Numer. Methods Eng.*, vol. 125, Apr. 2024, Art. no. e7478, doi: 10.1002/nme.7478.

[40] ANSYS, Inc., "Mesh deformation," in *ANSYS CFX-Solver Modeling Guide, Release 2023 R2*, Canonsburg, PA, USA: ANSYS, Inc., Jul. 2023, sec. 1.2.2, pp. 42–54.

[41] A.M. Malek et al., "Hemodynamic shear stress and its role in atherosclerosis," *JAMA*, vol. 282, no. 21, pp. 2035–2042, Dec. 1999, doi: 10.1001/jama.282.21.2035.

[42] X. Yuan et al., "Four-dimensional analysis of aortic root motion in normal population using retrospective multiphase computed tomography," *Eur. Heart J. Imag. Methods Pract.*, vol. 2, no. 1, Feb. 2024, Art. no. qyae007, doi: 10.1093/ehjimp/qyae007.

[43] T. Korpela et al., "Flow displacement and decreased wall shear stress might be associated with the growth rate of an ascending aortic dilatation," *Eur. J. Cardio- Thoracic Surg.*, vol. 61, no. 2, pp. 395–402, Feb. 2022, doi: 10.1093/ejcts/ezab483.

[44] A. Guala et al., "Wall shear stress predicts aortic dilation in patients with bicuspid aortic valve," *JACC Cardiovasc. Imag.*, vol. 15, no. 1, pp. 46–56, Jan. 2022, doi: 10.1016/j.jcmg.2021.09.023.

[45] G. Soulat et al., "Association of regional wall shear stress and progressive ascending aorta dilation in bicuspid aortic valve," *JACC Cardiovasc. Imag.*, vol. 15, no. 1, pp. 33–42, Jan. 2022, doi: 10.1016/j.jcmg.2021.06.020.

[46] S.P. Kauhanen, "Aortic dilatation associates with flow displacement and increased circumferential wall shear stress in patients without aortic stenosis: A prospective clinical study," *J. Magn. Reason. Imag.*, vol. 50, no. 1, pp. 136–145, Jul. 2019, doi: 10.1002/jmri.26655.

[47] F. Hammaréus et al., "Wall shear stress measured with 4D flow CMR correlates with biomarkers of inflammation and collagen synthesis in mild-to-moderate ascending aortic dilation and tricuspid aortic valves," *Eur. Heart J. Cardiovasc. Imag.*, vol. 25, no. 10, pp. 1384–1393, Oct. 2024, doi: 10.1093/ehjci/jeae130.

[48] A. Redheuil et al., "Age-related changes in aortic arch geometry: Relationship with proximal aortic function and left ventricular mass and remodeling," *J. Am. Coll. Cardiol.*, vol. 58, no. 12, pp. 1262–1270, Sep. 2011, doi: 10.1016/j.jacc.2011.06.012.

[49] R. Perinajová et al., "A comprehensive MRI-based computational model of blood flow in compliant aorta using radial basis function interpolation," *BioMed. Eng. OnLine*, vol. 23, no. 1, Jul. 2024, Art. no. 69, doi: 10.1186/s12938-024-01251-x.

[50] L. Geronzi et al., "Calibration of the mechanical boundary conditions for a patient-specific thoracic aorta model including the heart motion effect," *IEEE Trans. Biomed. Eng.*, vol. 70, no. 11, pp. 3248–3259, Nov. 2023, doi: 10.1109/TBME.2023.3287680.

[51] Y. Zhu et al., "A combined 4D flow MR imaging and fluid-structure interaction analysis of ascending thoracic aortic aneurysms," *Biomech. Model. Mechan.*, pp. 1–16, 2025, doi: 10.1007/s10237-025-01939-6.

[52] A. J. Barker et al., "Assessing wall stresses in bicuspid aortic valve-associated aortopathy: Forecasting the perfect storm?," *J. Thoracic Cardiovasc. Surg.*, vol. 156, no. 2, pp. 471–472, Aug. 2018, doi: 10.1016/j.jtcvs.2018.03.092.

[53] V. Bell et al., "Longitudinal and circumferential strain of the proximal aorta," *JAMA*, vol. 3, no. 6, Dec. 2014, Art. no. e001536, doi: 10.1161/JAHA.114.001536.

[54] A. Guala et al., "Proximal aorta longitudinal strain predicts aortic root dilation rate and aortic events in Marfan syndrome," *Eur. Heart J.*, vol. 40, no. 25, pp. 2047–2055, Jul. 2019, doi: 10.1093/eurheartj/ehz191.

[55] E. M. van Disseldorp et al., "Quantification of aortic stiffness and wall stress in healthy volunteers and abdominal aortic aneurysm patients using time-resolved 3D ultrasound: A comparison study," *Eur. Heart J. Cardiovasc. Imag.*, vol. 20, no. 2, pp. 185–191, Feb. 2019, doi: 10.1093/ehjci/jey051.

[56] A. Desyatova et al., "Effects of longitudinal pre-stretch on the mechanics of human aorta before and after thoracic endovascular aortic repair (TEVAR) in trauma patients," *Biomech. Model. Mechanobiol.*, vol. 19, no. 1, pp. 401–413, Feb. 2020, doi: 10.1007/s10237-019-01217-2.